ACS OMEGA

Open Access

http://pubs.acs.org/journal/acsodf

Article

ZIF-67 MOF-Derived Mn_3O_4 @ N-Doped C as a Supercapacitor Electrode in Different Alkaline Media

Amal F. Seliem, Ayeda Y. A. Mohammed, A. Attia, Salma Aman,* Naseeb Ahmad, and Mohamed M. Ibrahim

Cite This: *ACS Omega* 2024, 9, 17563−17576

Read Online

ACCESS | Metrics & More | Article Recommendations | Supporting Information

ABSTRACT: Transition-metal oxide has been identified as an auspicious material for supercapacitors due to its exceptional capacity. The inadequate electrochemical characteristics, such as prolonged cycle stability, can be ascribed to factors, such as low electrical conductivity, sluggish reaction kinetics, and a deficiency of active sites. The transition-metal oxides derived from the MOF materials offer a larger surface area with enriched active sites and a faster reaction rate along with good electrical conductivity. The manganese (Mn)-based metal−organic framework (MOF)-derived materials were produced using the pyrolysis method. Zeolitic imidazolate frameworks (ZIF-67) were fabricated in water at ambient temperature with the aid of triethylamine. Multiple techniques were used to examine the characteristics of the fabricated electrode materials. The influence of the electrolyte on the electrochemical activity of the Mn_3O_4@N-doped C electrode materials was determined in KOH, NaOH, and LiOH. For manufacturing of "Mn_3O_4@N-doped C", ZIF-67 was used as a precursor. The capacitive performance of the Mn_3O_4@N-doped C electrode increased as a result of nitrogen-doped carbon; after 5000th cycles, the electrode retained an excellent rate capability and a high specific capacitance (C_s) of 980 F g^{-1} at 1 A g^{-1} under 2.0 KOH electrolyte in a three electrode system. The carbonized manganese oxide displays also had a high C_s of 686 F g^{-1} in two electrode systems in 2.0 M KOH. Materials made from MOFs show promise as capacitive materials for applications in energy conversion storage owing to their straightforward synthesis and strong electrochemical performance.

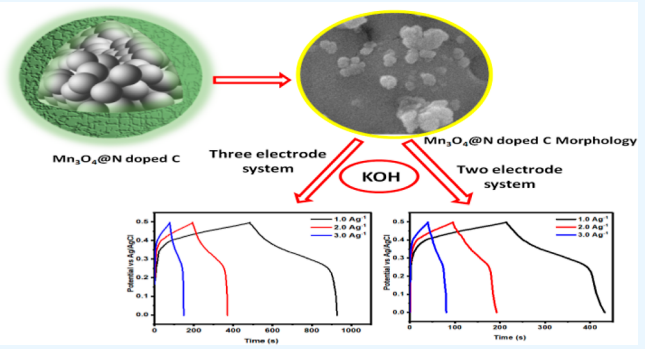

1. INTRODUCTION

Transition-metal oxides (TMOs) have larger theoretical capacitances because of the many oxidation states of transition metals (TMs). Therefore, several types of TMOs have been employed as potent electrocatalysts for supercapacitor (SC) electrodes.[1−3] These include binary metal oxides, Co_3O_4,[4] RuO_2,[5] NiO,[6] ZnO,[7] Mn_2O_3,[8] Fe_2O_3,[9] and Cu_2O.[10] Of these TMOs, Mn_3O_4 has garnered the greatest attention due to its extraordinarily high theoretical capacitance.[11−14] Due to its low electrical conductivity, Mn_3O_4 is not useful in practical settings. This makes it challenging to harness the material's electrochemical potential.[15,16] Adding carbon nanofibers,[17] graphene,[18] carbon nanotubes,[19] or amorphous carbon to Mn_3O_4 electrodes has been shown to improve electron and ion mobility. High electron and ion-transfer efficiencies may be achieved by fabricating nanostructured Mn_3O_4 materials, which improves electrochemical performance.[20−23] The majority of published ways to combine carbon with Mn_3O_4, however, need either lengthy processes or expensive carbon sources.[24−26]

Interesting porous coordination polymers called zeolitic imidazolate frameworks (ZIFs) combine metal cations with organic linkers (metal−organic frameworks or MOFs).[27,28] The framework architecture surface area and pore size may be readily controlled by an organic linker and metal positive ion.[29−32] The MOFs have been reported in a number of fields, such as CO_2 gas conversion,[33] water purification[34] and photocatalysis,[35] electronics and biomedicine,[36] and electrochemical biosensors.[37]

The excellent capacitive performance of MOx and MOFs made from MOFs depends on their uniform nanostructure, N_2 doping, high porosity, or rich carbon hybrids. To create porous Mn_3O_4 structures, Mn-based MOFs (Mn-MOFs) have been shown to be intriguing substrates.[38,39] Mixed-valence manganese (i.e., Mn_3O_4) is a potent candidate for SCs due to greater theoretical capacitance, simplicity in production and abundance of redox processes.[40] Various researchers have

Received: January 20, 2024
Revised: March 17, 2024
Accepted: March 21, 2024
Published: April 7, 2024

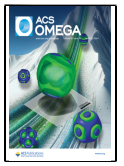

https://doi.org/10.1021/acsomega.4c00676
ACS Omega 2024, 9, 17563−17576

synthesized MOF-derived metal oxides, such as Ruoyu Wang et al.[41] which developed the Mn_3O_4@C/rGO nanocomposite and analyzed their potential capability for energy-saving applications. The results revealed that the Mn_3O_4@C/rGO exhibited 328.6 F cm^{-2} high C_s, revealing the efficiency for supercapacitor applications. Zhao et al.[42] used a simple carbonization of Mn-MOFs with poly(styrene-*co*-AA) spheres to develop a Mn_3O_4@N-doped C/graphene nanocomposite. In a 1.0 M Na_2SO_4 electrolyte solution, the Mn_3O_4@N-doped C/graphene (MCG) exhibits exceptional electrochemical capabilities, with maximal specific capacitances of 456 and 246 F g^{-1} @ 1 and 20 A g^{-1}. Additionally, the Mn_3O_4@N-doped C/graphene exhibits excellent cycling life, 98.1% of the capacitance @ 5 A g^{-1} after 2000 cycles. Babak Rezaei et al.[43] synthesized the three-dimensional pyrolytic carbon/Mn_3O_4 nanostructure via wet chemical deposition for energy conversion devices. The use of MOF-derived materials as effective sacrificial templates or precursors for producing different porous carbon, metal compounds, and composites have been studied.[44−48] The novelty of the work includes the material made from MOFs to maintain the morphology and form of the original MOFs. Carbon, nitrogen-doped carbon, porous metal oxides, and nanohybrid may all be produced by the heating method. The electrochemical performance of electrodes made of Mn_3O_4 may be improved by carbon doping.[49,50] Moreover, the electrochemical features of prepared samples were also investigated by using three different electrolytes (KOH, NaOH, and LiOH), and better results were obtained by using the KOH electrolyte because of its smaller hydration sphere which causes increase in the migration rate of ions. The fabricated materials exhibited very good retention capacitance and longer life stability of >92%. All of the ascribed information suggests that MOF-derived metal oxide exhibited high C_s and other fascinating electrical features inspired to develop MOF-derived MOx for supercapacitor applications.

Herein, triethylamine (TEA) was used to help create the porous construction of ZIF-67, which contains meso- and microporous regimes. Mn_3O_4 embedded in N-doped carbon was prepared using the fabricated product as a precursor (Mn_3O_4@N-doped carbon). At ambient temperature, H_2O is used as a solvent during the fabrication process. The supercapacitor's electrode material was Mn_3O_4@N-doped carbon and measured its electrochemical applications in different basic electrolytes, such as NaOH, LiOH, and KOH. The electrochemical result revealed that the MOF-derived electrocatalyst exhibited the high C_s in KOH than other basic electrolytes. Furthermore, the longer life cycles also indicate the longer stability of the fabricated electrode compared to other reported materials.

2. EXPERIMENTAL SECTION

2.1. Fabrication of ZIF-67 and Mn_3O_4@N-doped C. All of the reagents used in the *ZIF-67 and Mn_3O_4@N-doped C* fabrication were purchased from Sigma-Aldrich. The TEA (Sigma-Aldrich, ≥99.5%)-assisted approach was used to complete the ZIF-67 synthesis procedure. In a nutshell, 6.9 mmol of 2-methyl imidazole (Hmim, Sigma-Aldrich, 99%) as a source of nitrogen was added after 7.4 mmol of TEA (1 mL) was inserted to 0.68 mmol of manganese nitrate under the vigorous stirring for 60 min. The precipitates were separated and then washed several times with H_2O and absolute C_2H_5OH (Sigma-Aldrich, 99.99%) solution. The material was dehydrated in an electric oven set to 85 °C naturally. Mn_3O_4@N-doped C was created by using ZIF-67. The material was heated to 700 °C in a crucible for 4 h in a muffle oven. The Mn_3O_4@N-doped C was rinsed twice, once with H_2O and once with C_2H_5OH (each 20 mL wash). The schematic procedure for the fabrication of carbonized metal oxide and ZIF-67 is illustrated in Scheme 1. The physiochemical and electrochemical studies of the synthesized material are provided in the Supporting Information.

Scheme 1. Fabrication of ZIF-67 and Mn_3O_4@Nitrogen-Doped C

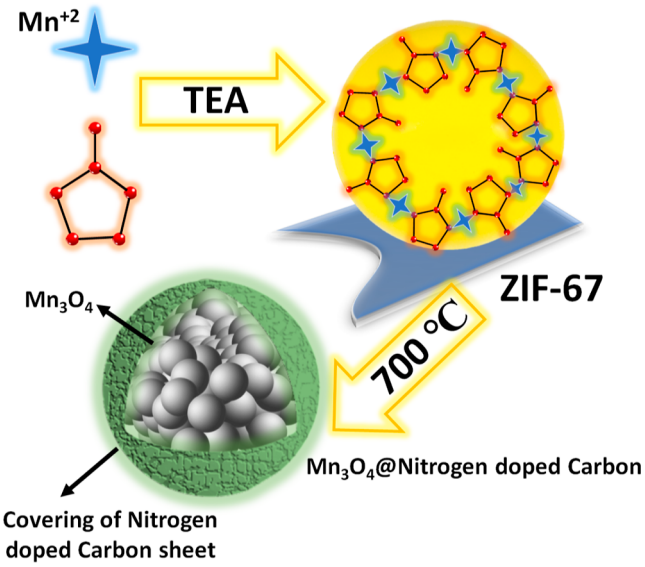

3. RESULTS AND DISCUSSION

3.1. Physiochemical Evaluation. X-ray diffraction (XRD) of fabricated ZIF-67 is well consistent with the simulated XRD for ZIF MOFs (CSD no.: GITTOT02), space group of *I*43*m* (217), and cell parameter of $\alpha = \beta = \gamma = 90°$ and $a = b = c =$ 16.9077 Å and is well matched with the previous report,[51] suggesting that the pure phase was synthesized without any additional peaks for any unwanted phases, as illustrated in Figure 1a. Furthermore, Figure 1b displays the Braggs angles of successful formation of 28.76, 32.34, 35.87, 37.81, 44.55, 50.74, 58.35, 59.95, and 64.55° corresponds to *hkl* indexes of (112), (103), (211), (004), (213), (105), (321), (215), and (323), respectively, which are well consistent with the JCPDS no. 01-080-0382. The crystallographic parameter of Mn_3O_4@N-doped C exhibited a tetragonal crystal system, space group of 141/*amd*, and space group number of 141 with a crystal parameter of $a = 5.76$, $b = 5.76$, and $c = 9.44$ Å. The presence of all the peaks confirms the effective synthesis of Mn_3O_4@N-doped C and the presence or absence of peaks confirm the pureness of the materials. The lack of a significant band for "C" indicates the low concentration or amorphous state of carbon in the final product following carbonization.

The structural analysis and surface functionalities of ZIF-67 MOF and carbonized-doped manganese oxide nanoarray were further confirmed by Fourier transform infrared (FT-IR) of 4000 to 500 cm^{-1}, as represented in Figure 2a. The transmittance band that appeared at 3010−3714 cm^{-1} in both fabricated materials is related to the hydroxyl stretching vibration mode of H_2O that are adsorbed on interfaces of

https://doi.org/10.1021/acsomega.4c00676
ACS Omega 2024, 9, 17563−17576

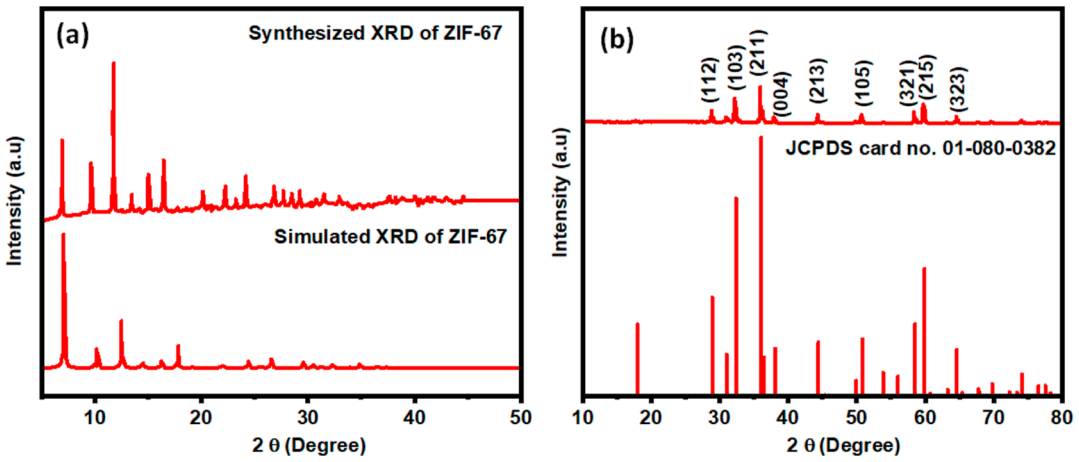

Figure 1. XRD of (a) ZIF-67 and (b) Mn_3O_4@N-doped C.

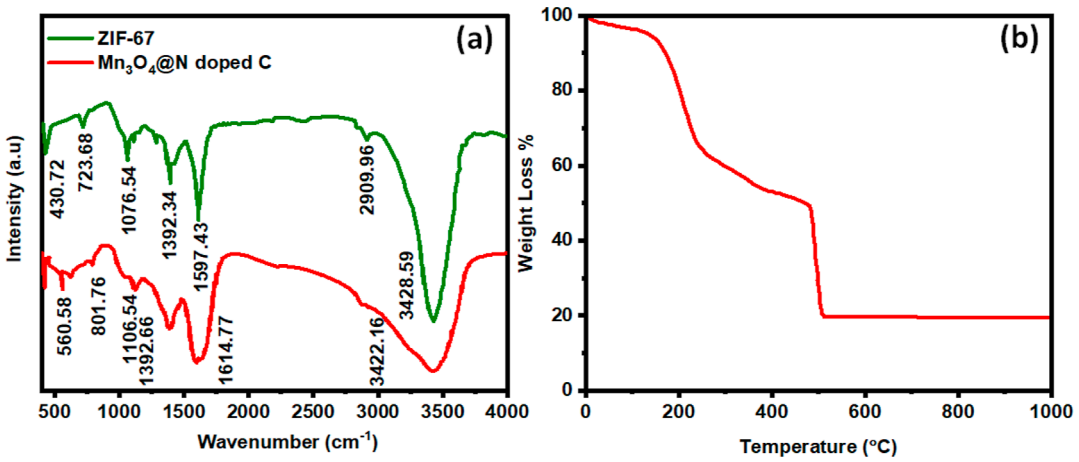

Figure 2. (a) FT-IR analysis of the ZIF MOF and carbonized manganese oxide and (b) TGA curve of the ZIF MOF.

electrocatalyst. The FT-IR spectrum of ZIF-67 display reflection bands in the range of 2909.96 cm^{-1} are owing to the C−H stretching band in the aliphatic chain and aromatic structure in 2-methylimidazole. The distinct transmittance bands at 1597.43, 1392.34, and 1076.54 cm^{-1} are owed to the imidazole ring and 723.68 cm^{-1} corresponds to a carbon nitrogen double bond in ligand 2-methylimidazole.[52] The FTIR peak detected at 430.72 cm^{-1} is related to the Mn−N bond.[53] The existence of distinctive peaks confirms the successful fabrication of ZIF-67 MOF. The Mn_3O_4@N-doped C display the characteristic peaks at 1614.77, 1392.66, and 1106.54 cm^{-1} are associated with nitrogen and carbon stretching bonds like C−N, C═C, and C−C, and the bands appeared below 1000 cm^{-1} are characteristic peaks of metal oxide (Mn−O) stretching bands. Their analysis is well consistent with the XRD analysis with no extra peaks revealing the purity of the fabricated materials. Figure 2b illustrates the thermogravimetric analysis (TGA) curve of fabricated ZIF MOFs measured under a nitrogen environment. The preliminary stages of mass reduction of 38% below the 250 °C and 16% from 490 °C are attributed to the elimination of potential guest species, such as solvents, nitrates, surface moisture, and physically attached linker species, respectively. The last phase found at 490 °C can be measured by the pyrolysis of organic groups and ZIF-67 nanostructure.

Scanning electron microscopy (SEM) microanalysis was employed to examine the morphology of both synthesized material at 500 nm. The SEM analysis of ZIF-67 revealed the rhombic dodecahedron morphology are displayed in Figure 3a. The present morphology of ZIF-67 also confirms the successful formation of ZIF-67 MOF. The Mn_3O_4@N-doped C exhibited an irregular spherical morphology, as represented in Figure 3b. The irregular shape Mn_3O_4@N-doped C exhibited a greater number of active regions that are more desirable for supercapacitive applications. The internal morphology of synthesized ZIF-67- and Mn_3O_4@N-doped C was investigated with transmission electron microscopy (TEM) analysis at 300 nm. The results revealed that ZIF-67- and Mn_3O_4@N-doped C exhibited the rhombic dodecahedron and nanoparticles, respectively, labeled with a yellow mark, as illustrated in Figure 3c,d. ZIF-67 and Mn_3O_4@N-doped C nanoarrays were employed to determined N_2 sorption isotherms, BET specific surface area (SSA), and the characteristic parameter of porous features. This work is illustrated Figure 3e,f, which suggests the type I−IV hybrid isotherms related to IUPAC classification and demonstrates the coexistence of porous states.[54] The obtained SSA values were 615 and 160 m^2 g^{-1} for ZIF MOFs and carbonized manganese oxide, respectively. Furthermore, the Barrett, Joyner, and Halenda technique was employed to investigate the size of pores of 1.45 and 6.45 nm for ZIF MOFs and carbonized manganese oxide, respectively.

In order to better understand the material's properties, the electronic states and chemicals of the structure were measured

https://doi.org/10.1021/acsomega.4c00676
ACS Omega 2024, 9, 17563−17576

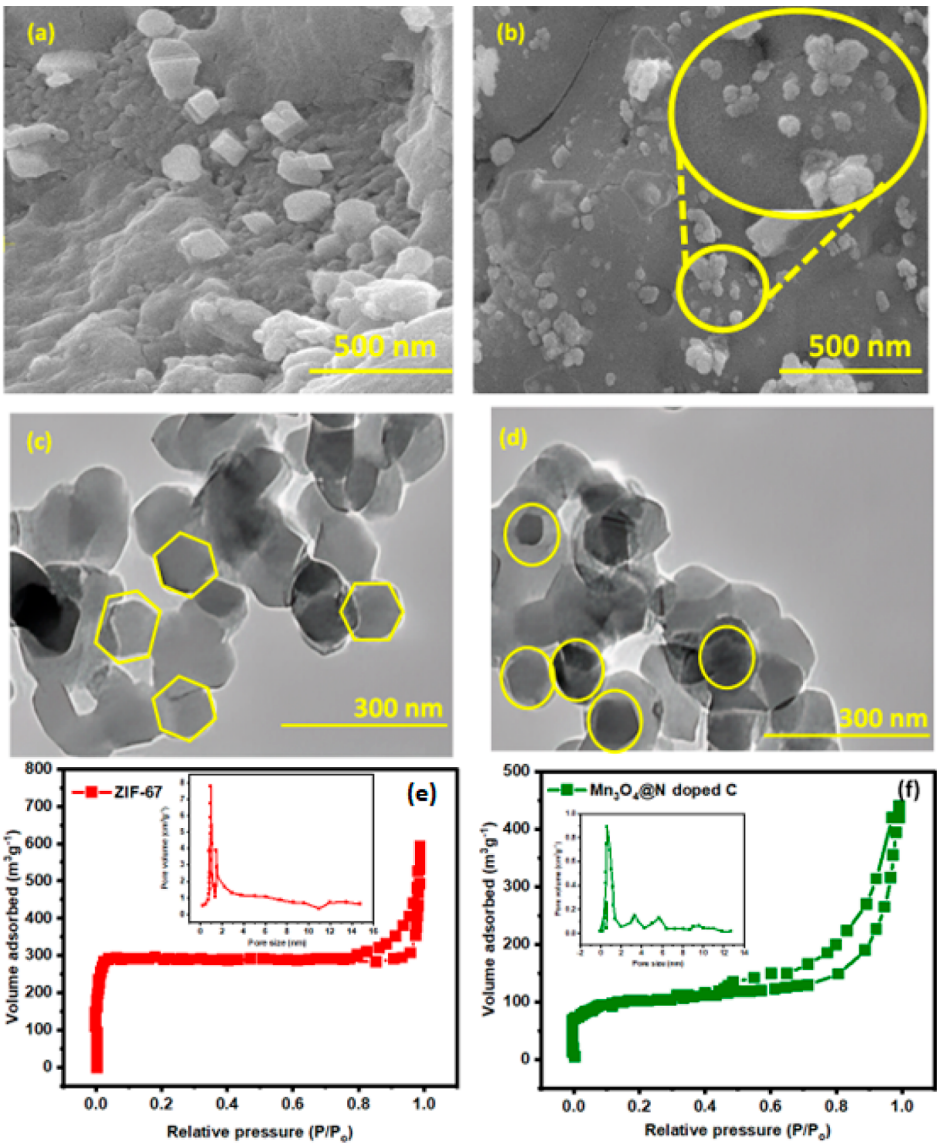

Figure 3. SEM micrograph of (a) ZIF MOF and (b) carbonized manganese oxide, TEM analysis of (c) ZIF MOF, (d) carbonized manganese oxide, and BET of (e) ZIF MOF and (f) Mn_3O_4@N-doped C.

using XPS. The compilation of all the elements found in Mn_3O_4@N-doped C from the overall scan is shown in Figure 4a. Using a Gaussian model, high-resolution scans of the component element peaks are represented in Figure 4b−d. The carbon spectrum Figure 4b displays the three peaks for C−C, O−C, and O−C═O related to 284.03, 285.5, and 288.38 eV, correspondingly. The N 1s display the XPS peaks at 399.42, 401.77, 403.45, and 407.06 cm^{-1} are corresponding to −N═C−, −N−, −HN−C−, and −HN−C═O, correspondingly. The oxygen 1s spectrum exhibited the XPS band at 528.74 and 531.2 eV owing to Mn−O and C═O and are displayed in Figure 4d. Mn 2p (Figure 4e) represents the two deconvoluted curves at 654.4 and 649.9 eV owing to Mn $2p_{1/2}$ and Mn $2p_{3/2}$, correspondingly. Further, the presence of no other peaks confirms the purity of the materials.

3.2. Electrochemical Evaluation for Supercapacitive Application. Mn_3O_4@N-doped C and ZIF-67 was subjected to a wide range of electrochemical studies to investigate the electrochemical performance in different electrolytes. Cyclic voltammetry (CV) analysis may be used to get a qualitative understanding of the electrochemical application taking place in the material and whether or not they are faradic in nature. First, it is important to make sure the electrode and electrolyte are compatible before investigating the material's electrochemical behavior. Capacitance changes as electrolyte ions are either removed from or absorbed by the electrode substance. Functionality of an electrolyte is significantly affected by the diffusion rate and the size of the solvated ions present.

The electrochemical characteristics of the carbonized manganese oxide electrode (thickness = 1.7 mm) have been investigated using a three-electrode configuration (CHI660e). Figure 5a−c displays the CV peak of Mn_3O_4@N-doped C in three distinct electrolyte media, such as 2.0 M lithium hydroxide, sodium hydroxide, and potassium hydroxide at different sweeping speeds (5−30 mV s^{-1}). Mn_3O_4@N-doped C exhibits a pair of redox curve in all electrolytes, which help to explain the pseudocapacitive nature.[55] These redox curves are brought on by the reduction and oxidation processes. Peak potentials for reduction and oxidation in a potassium hydroxide solution are similar to those in carbonized

https://doi.org/10.1021/acsomega.4c00676
ACS Omega 2024, 9, 17563−17576

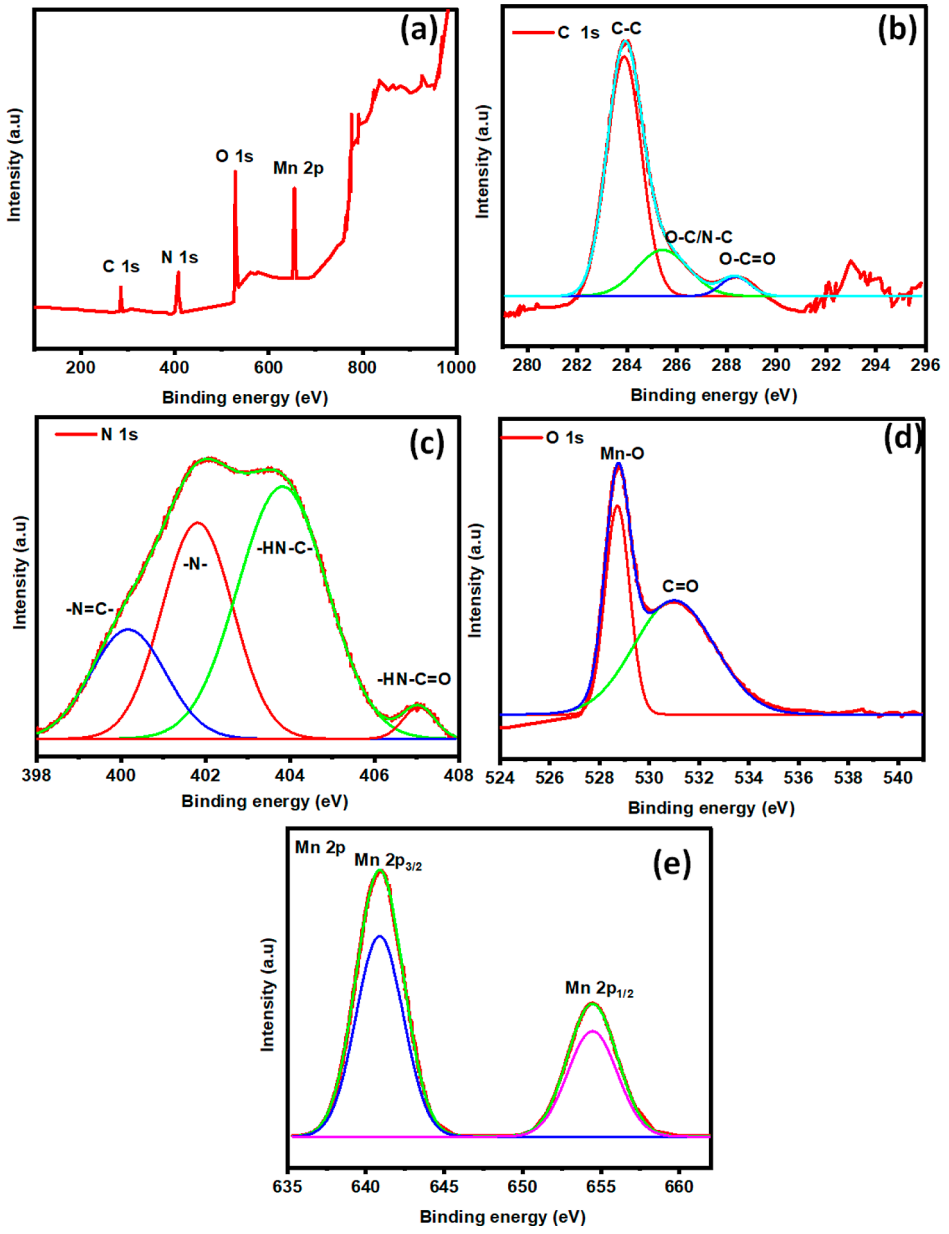

Figure 4. XPS spectra of (a) width survey, (b) carbon 1s, (c) nitrogen 1s, (d) oxygen 1s, and (e) Mn 2p spectrum.

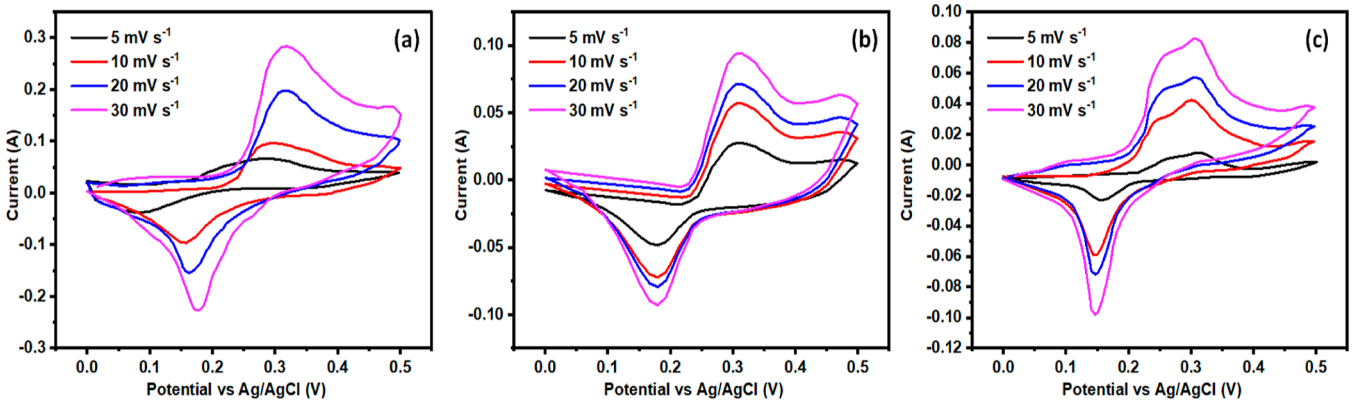

Figure 5. CV curve of Mn_3O_4@N-doped C in a variety of electrolytes (a) KOH, (b) sodium hydroxide, and (c) LiOH.

manganese oxide electrolytes. The reaction of metal oxide in the electrolyte ion is represented in eq 1.

$$Mn_3O_4 + OH^- + H_2O \rightarrow MnOOH + e^- \quad (1)$$

https://doi.org/10.1021/acsomega.4c00676
ACS Omega 2024, 9, 17563−17576

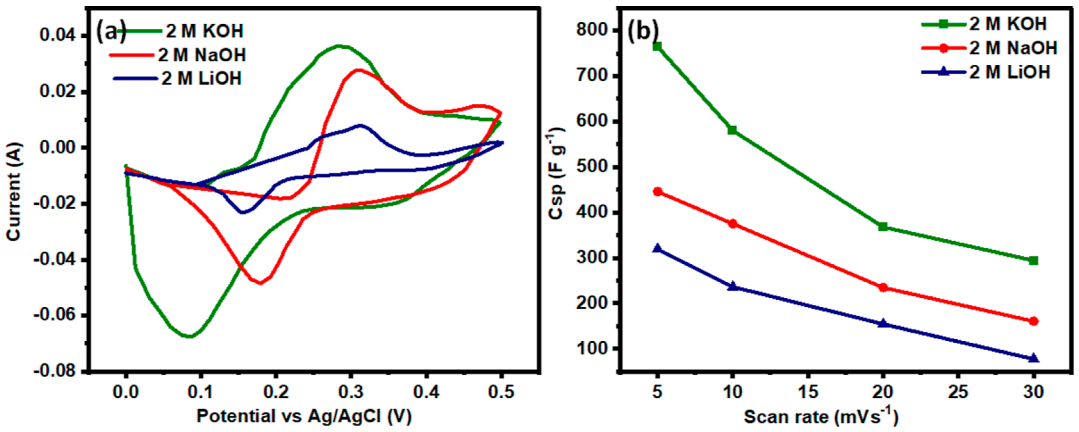

Figure 6. Comparative analysis of (a) CV and (b) C_s plots in a variety of electrolyte.

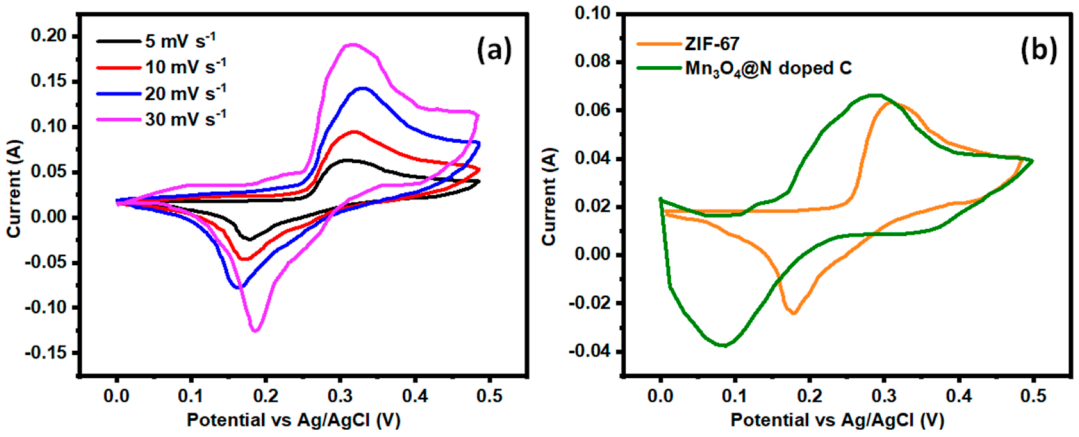

Figure 7. (a) CV of ZIF MOF and (b) comparison between the ZIF MOF and carbonized manganese oxide.

The reduction of Mn^{3+} to Mn/Mn^{2+} metal and the oxidation of metal Mn/Mn^{2+} to Mn^{3+}, correspondingly, are responsible for the reduction peaks appearing at approximately 0.083 V and the oxidation band at 0.28 V at 5 mV s^{-1} in the potassium hydroxide electrolyte. All curves that deviate from the perfectly rectangular form are said to exhibit pseudocapacitive behavior. As can be observed in Figure 5, the cathodic and anodic peaks move to lower and higher potentials, respectively, as a result of the scan rate rising, which is a result of the restricted ion movement during oxidation reduction processes. The CV peaks for carbonized materials in the 0.0−0.5 V in alkaline electrolytes are shown in Figure 5 at different scanning rates. Compared to the carbonized manganese oxide in potassium hydroxide, lithium hydroxide, and sodium hydroxide electrolytes, the capacitance of the carbonized manganese oxide in the KOH electrolyte is bigger because of the stronger redox characteristics and CV polygonal area. The current responsiveness of carbonized manganese oxide declines in different electrolytes in the sequence of KOH < NaOH < LiOH.

According to the reported research, the cations (Na^+, Li^+, and K^+) tend to form hydrated ions in water containing electrolytes. When a larger ion is hydrated, a wider variety of hydrated ions is commonly produced, but a higher quantity of hydrated ions is frequently produced when a smaller ion is hydrated. The larger K^+ and Na^+ cations produce lesser hydrated ions with radii of 3.31 and 3.58 nm, correspondingly, while the lesser Li^+ cation produces a greater hydrated ion with a radius of 3.82 nm. That is why the specific capacitance is greater when 2.0 M KOH is used as the electrolyte rather than NaOH or LiOH.[56] The reported conductivity of K^+ ions at 25 °C is larger than that of sodium ions at 50 °C and Li^+ ions at 38 °C, suggesting that K^+ would have a higher ion mobility. Improved electrochemical performance is the consequence of greater ionic mobility and contact with the electrode material due to the K^+ ions' reduced hydration radius. The fact that K^+ ions gained a small charge density, indicating poor solvation attraction with H_2O species, allows for improved polarization during the desolvation processes. This is an additional advantage of K^+ ions. In redox processes, this enables K^+ ions to readily enter the electrode. The results mentioned above show that cations play a crucial function in electrochemical processes.

The CV comparison with the effect of different electrolytes on carbonized manganese oxide are displayed in Figure 6a. The comparative analysis revealed that the Mn_3O_4@N-doped carbon exhibited a high current density in KOH with a larger polygonal area than LiOH and NaOH. The variations in C_s values with sweeping speed for various electrolytes are illustrated in Figure 6b. The material capacitance reduces with increased scan speed, which may be due to a reduction in the greater number of active regions engaged in oxidation and reduction processes. This relationship demonstrates the total number of active redox reaction sites. The greater number of reduction and oxidation regions participating at smaller sweeping rates is greater than at larger scan rates. Low scan rates would provide the ions sufficient time to reach the

https://doi.org/10.1021/acsomega.4c00676
ACS Omega 2024, 9, 17563−17576

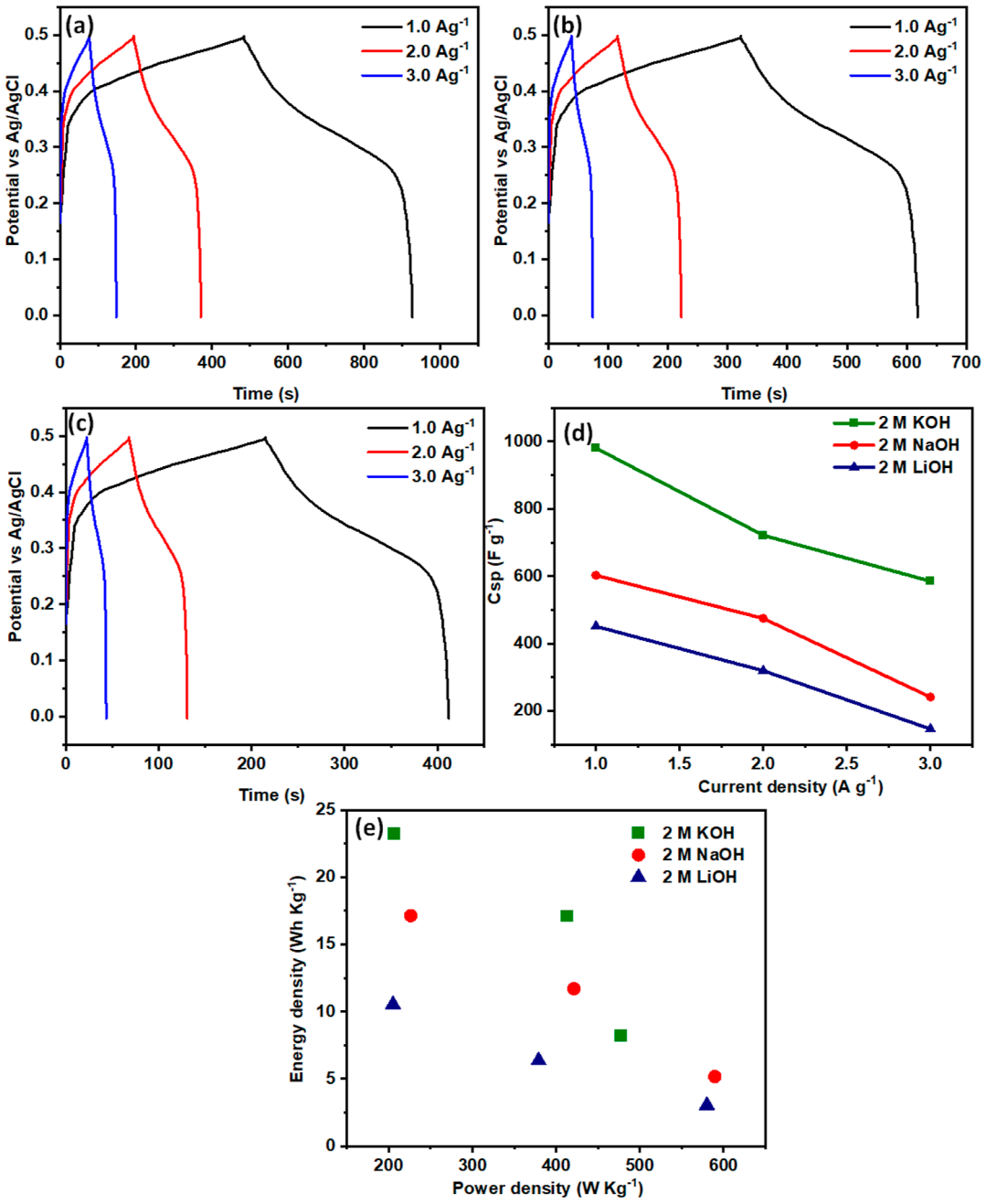

Figure 8. GCD analysis of 2.0 M (a) KOH, (b) NaOH, (c) LiOH, (d) C_s plot profile, and (e) Ragone plot profile of carbonized manganese oxide in different electrolytes.

electrode interface, enabling the deep penetration of electrolyte ions on the active site of interface materials. Only the surface adsorption process happens at a faster sweeping speed because the electrolyte ions do not have sufficient time to adsorb the substance. The 2.0 M potassium hydroxide electrolyte has the largest capacitance compared to the sodium hydroxide and lithium hydroxide electrolytes because K^+ ions may easily access the inner surface of the electrocatalyst materials.

For comparison purposes, the CV analysis of ZIF-67 was conducted under the same electrochemical conditions in 2.0 M KOH as described for Mn_3O_4@N-doped C at 5−30 mV s^{-1}. The ZIF-67 exhibited the C_s of 432.16, 303.96, 171.92, and 143.27 F g^{-1} for 5−30 mV s^{-1} calculated with eq. S1. Furthermore, the ZIF-67 displays a maximum current of 0.177 A for 30 mV s^{-1}, as represented in Figure 7a. The comparison between the CV curve of ZIF MOF and carbonized manganese oxide is displayed in Figure 7b. The comparative analysis suggests that the ZIF-67 exhibited a small polygonal area and smaller current compared to Mn_3O_4@N-doped C resulting in small C_s. The redox peak indicates the pseudocapacitive behavior of the synthesized material. The redox peak was responsible for the transition of Mn^{2+}/Mn^{3+}.[57]

Studies of charge−discharge behavior in 2.0 M KOH, LiOH, and NaOH electrolytes are employed to understand more about the electrochemical features of the Mn_3O_4@N-doped C material, which works best in the 2.0 M KOH electrolyte concerning capacitance. The galvanostatic charge−discharge (GCD) of carbonized manganese oxide is illustrated in Figure 8a−c at different current densities, such as 1, 2, and 3 A g^{-1}. The electrochemical reaction is driven by a redox mechanism,

https://doi.org/10.1021/acsomega.4c00676
ACS Omega 2024, 9, 17563−17576

as suggested by the nonlinearity of the discharge curve, which agrees with the cyclic voltametric results. A smaller current density results in a slower discharge of the material, whereas a higher current density results in a faster discharge, as shown by the graph. The C_s increases in proportion to the square of the discharge period. As a result, the C_s grows at a small current density (C.D.) and is reduced at high densities. According to the discharge curve's nonlinear nature, a redox mechanism drives the electrochemical reaction, which is in line with the CV findings. The graph shows that while the C.D is low, the material discharges more slowly, and as the current density rises, the material discharges more quickly. As the discharge time increases, the C_s rise. The C_s thus increases at smaller C.D. and less as C.D increases.

Mn_3O_4@N-doped C exhibits nonlinear discharge and asymmetrical behavior. Pseudocapacitance was due to reversible interactions between electrolyte ions and rich surface heteroatoms, as shown by deviations from triangular shapes in the GCD curves. C_s values for carbonized carbon in potassium hydroxide, lithium hydroxide, and sodium hydroxide @ of 1, 2, and 3 A g^{-1} are 980.64, 721.55, and 584.90 F g^{-1}, 451.22, 319.47, and 146.47 F g^{-1} and 602.65, 474.72, and 241.22 F g^{-1}, respectively, as measured in eq S2, and their comparison with the reported literature is given in Table 1.

Table 1. Comparative Analysis among the Published MOF-Derived and -Synthesized Materials

Sr no	materials	specific capacitance (F g^{-1})	current density (A g^{-1})	electrolyte	ref
1	ZIF-derived N-doped porous carbon-ZS	285.8	0.1	6.0 M KOH	58
2	RhB@ZIF-8-derived ZnO@C	1200	1.0	2.0 M KOH	27
3	ZIF-derived ZnS/CoS	1646	1.0	6.0 M KOH	59
4	ZIF-8-derived ZnO/C@f-MWCNT	650	1.0	3.0 M KOH	60
5	ZIF-8 derived ZnS@C	145.7	2.0	1.0 M Na_2SO_4	61
6	ZIF-8 derived N-doped PC-CNTs	250	0.1	6.0 M KOH	62
7	HPZIF-67-derived Co_3O_4@N-doped C	709	1.0	2.0 M KOH	20
8	MOF-derived $ZnMn_2O_4$/C	589	1.0	1.0 M Na_2SO_4	63
10	ZIF-8-based carbon@MnO_2	247.9	0.5	2.0 M Na_2SO_4	64
11	**ZIF-67 MOF-derived Mn_3O_4@N doped C**	**980**	**1**	**2.0 M KOH**	**this work**

Furthermore, a comparative analysis among the C_s of Mn_3O_4@N-doped C in the different electrolytes is given in Figure 8d. Specific capacitance is observed to be smaller with increasing C.D. This is linked to increased ionic resistance and decreased charge diffusion into the inner active sites. The main factor for the reduction at higher current densities is an increased voltage (*IR*) drop, which often occurs in transition-metal oxides. The capacitance decreases with increasing current density, which may be explained by the sample's delayed response to abrupt changes in current and potential. At 1 A g^{-1}, the diffusion of electrolyte ions can reach the whole interface of the electrode material, resulting in an increase in the C_s. Increases in current density cause a decrease in capacitance because they lessen the effective intercalation between the electrode and electrolyte ions. The Ragone plot was used to display the relationship among the energy density (E_d) and power density (P_d) in Figure 8e and measured with the help of eqs S3 and S4.

The GCD curve of ZIF-67 GCD in 2.0 M potassium hydroxide solutions with C.D of 1, 2, and 3 is illustrated in Figure 9a. The C_s of ZIF-67 is observed in the range of 519.88, 410.66, and 257 F g^{-1} @ 1, 2, and 3 A g^{-1}. The GCD curves of both ZIF MOF and carbonized manganese oxide are displayed in Figure 9b, suggesting that the doped material displays a longer discharge time than the MOF. The result revealed that the carbonized manganese oxide has a greater discharge time than the ZIF MOF, resulting in higher C_s. "N" different atoms, which improve the gravimetric efficiency of carbon-based supercapacitors, may be the cause for the rise in C_s. Capacitance and rate performance of energy storage devices have both increased dramatically as a consequence of improved electrolyte accessibility and carbon wettability, as well as enhanced pseudocapacitance given by "N" doping. Figure 9c displays the comparison between the GCD profile of Mn_3O_4@N-doped C in the different electrolytes. The results suggest that the N-doped material exhibited the 2.0 M KOH having the longest discharge curve compared to that of another alkaline electrolyte that gives high C_s.

The electrochemical impedance spectroscopy (EIS) Nyquist plot displays the association among the imaginary and real parts of impedance (Z' and Z'') in the range of 0.1 to 100 000 Hz. The starting frequency of EIS is 0.1 Hz and ending frequency is 100 000 Hz. The Mn_3O_4@N-doped C Nyquist curve in different alkaline electrolytes is given in Figure 10a. All electrolytes have a characteristic impedance profile known as Warburg impedance, which consists of a linear region with a depressed circle in the greater frequency range. The slope line present in the low-frequency region of Nyquist plot indicates Warburg impedance displaying the diffusion process and the slope line toward 45° indicates the faster diffusion of electrolyte ions.[65,66] However, the slope line of KOH in Mn_3O_4@N-doped C toward 45° indicates the more capacitive nature and faster diffusion of OH^- electrolyte ions on the electrode surfaces than the other electrolyte solution. The small depressed circle shows the charge-transfer resistance (R_{ct}) of the electrocatalytic materials. The measured R_{ct} values for Mn_3O_4@N-doped C in potassium hydroxide, sodium hydroxide, and lithium hydroxide are 2.35 , 5.63 , and 8.31 Ω, respectively. The results suggest that KOH exhibited a small R_{ct} value than NaOH and LiOH, which might be attributed to the conductive nature and diverse morphology of Mn-doped material than the carbonaceous MOFs.

The chronoamperometry analysis (Figure 10b) was used to examine the stable behavior of Mn-doped material in potassium hydroxide at 0.75 V. The results revealed that the Mn-doped material showed a very small decline in the current density in the first few hours, and then they showed a straight line up to 50 h. The slight decline was due to the activation of active sites, and a straight line indicates stable behavior than the benchmark (RuO_2). To determine the electrochemical stability of carbonized manganese oxide, galvanostatic charge−discharge studies are performed. Mn_3O_4@N-doped C was evaluated @ 1 A g^{-1} for 5000th cycles, and the analysis is displayed in Figure 10c. Mn_3O_4@N-doped C also shows the retention capacitances of 97.77, 95.54, and 88.41% in the

https://doi.org/10.1021/acsomega.4c00676
ACS Omega 2024, 9, 17563−17576

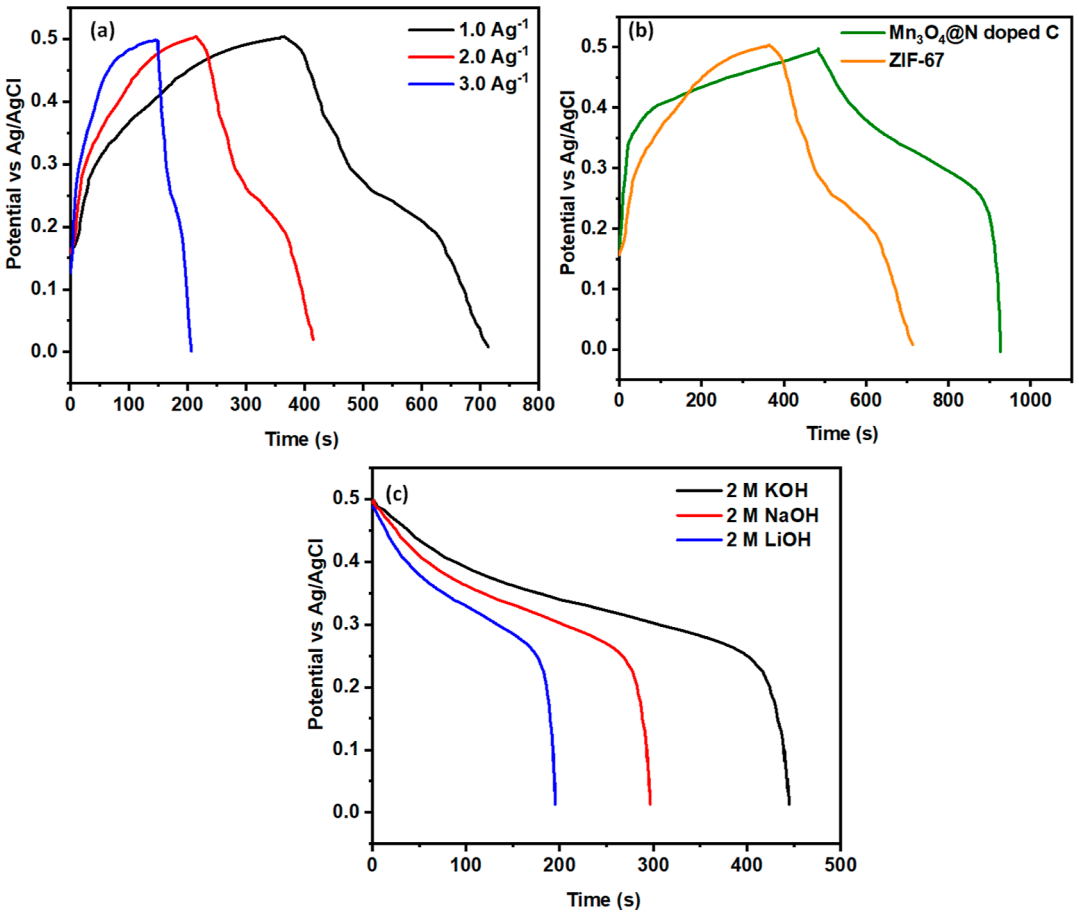

Figure 9. (a) GCD curve of ZIF-67, (b) comparison between the ZIF MOF and carbonized manganese oxide, and (c) comparison of Mn_3O_4@N-doped C among the different electrolytes.

electrolyte of KOH, NaOH, and LiOH. The high-rate capability of N-doped carbon facilitates ion transport in a large number of porous states. The cycling stability of doped material materials was determined with CV analysis under a KOH solution, as represented in Figure 10d. The CV analysis shows the very small change in the current density of indicates the cyclic stability of the synthesized products.[67,68] The structural stability of the Mn_3O_4@N-doped C was evaluated with XRD analysis to confirm the lattice property of the materials. The XRD pattern (Figure 10e) of doped materials displays reduction in intensity, and the absence of some diffraction peaks is attributed to blockage of some active zones and destruction of some active sites that cannot perform the catalytic activity.

3.3. Two-Electrode Evaluation. The real-time potential capability of Mn-doped materials as supercapacitor electrodes was evaluated with two electrode systems with GCD and CV profile analyses in a potassium hydroxide solution. Figure 11a displays the CV curve having a more significant current of 0.10 A with a different sweep speed of 5−30 mV s^{-1}. All of the CV peaks show the quasi-symmetrical shape at a larger scanning speed at 30 mV s^{-1}, displaying good retention capacitance and ideal capacitive behavior. The analysis revealed that the current rises with the rise of sweeping speed, as it is directly linearly proportional to the sweeping rate. Figure 11b displays the C_s profile obtained from CV analysis, which suggests that the C_s values of the obtained materials declined with the increase in sweeping speed. The highest C_s was obtained in a small sweeping speed of 432.16 @ 5 mV s^{-1}. It was attributed to the short time available at a high scan rate for the intercalation of KOH ions to the surface of the electrocatalyst. The GCD profile analysis of Mn-doped material displays the nonlinear curve, as demonstrated in Figure 11c. The outcomes revealed that the Mn-doped material at 1 A g^{-1} exhibited a more significant discharge curve, indicating the good capacitive properties of the material at a small current density. Further, GCD analysis (Figure 11d) was employed to investigate the C_s with eq S2, which was found in the range of 686.27, 523.80, and 367.5 F g^{-1} @ 1, 2, and 3 A g^{-1} and the relationship between the C_s and current density. The gradual decline in the C_s of Mn-doped material with rising current density was due to less time for electrolyte ions to penetrate the depth of the electrode materials. Based on our experimental results, the produced Mn_3O_4 @ N-doped C nanostructures constitute a promising electrocatalytic nanostructure for a more significant-performance symmetrical electrode materials, with higher capacitive performance than previously published electrodes. This research focuses on supercapacitor properties with two and three electrodes. The three-electrode system outperformed the two-electrode technique in terms of the electrochemical efficiency. Mobile electrolyte ions have unrestricted access to the electrode material during a charge storage process, resulting in a very high C_s response, which may result from an electrode being exposed to an excessive quantity of potassium hydroxide solution. A three-electrode chemical cell architecture, while theoretically conceivable, is unsuitable for

https://doi.org/10.1021/acsomega.4c00676
ACS Omega 2024, 9, 17563−17576

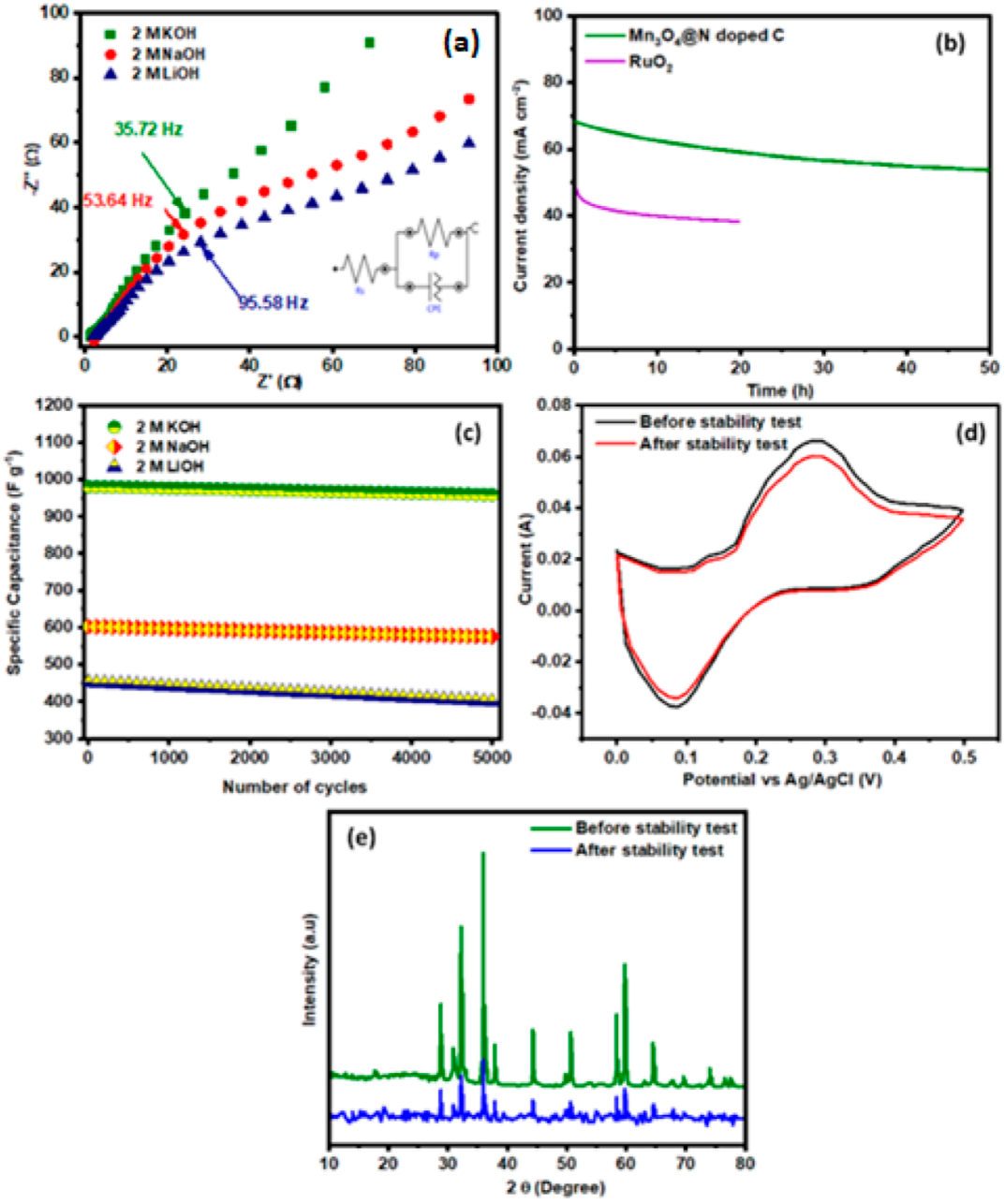

Figure 10. (a) EIS profile of carbonized manganese oxide in different electrolytes, (b) chronoamperometry analysis in KOH, (c) GCD rate capability comparative analysis in different electrolytes, (d) cyclic stability in KOH, and (e) XRD of Mn_3O_4@N-doped C.

real-world applications because commercial supercapacitors are built using a two-electrode structure. By using only two electrodes, we can reduce the volume of electrolyte ions, allowing for the low-cost mass production of supercapacitors. The C_s of Mn_3O_4 @ N-doped C is observed to be lower (686 F g^{-1}) in a two-electrode system as compared to the three-electrode system (980 F g^{-1}) due to the polarization of the symmetric electrode. The combined effects of Mn_3O_4 and N-doped C and high surface area all contribute to excellent electrochemical performance.

4. CONCLUSIONS

The fabrication of a porous ZIF MOF was made with a TEA-assisted technique. The fabricated ZIF-67 was employed as a precursor to generate carbonized manganese oxide via a pyrolysis of one-step carbonization. The effect of the different electrolytes, such as potassium hydroxide, lithium hydroxide, and sodium hydroxide on the capacitive properties of the Mn_3O_4@N-doped C was also investigated in this study. Their electrochemical analysis revealed that Mn_3O_4@N-doped C displays a high electrochemical efficiency of 980 F g^{-1} in potassium hydroxide, which is larger than the other basic electrolyte solution. Further, the comparative analysis was conducted with ZIF-67 and Mn_3O_4@N-doped C in 2.0 M KOH solution, and their electrochemical analysis suggested that Mn_3O_4@N-doped C exhibited higher C_s of 980 F g^{-1} than ZIF-67 (686 F g^{-1}). The EIS results display the smaller R_{ct} value of 2.35 Ω for Mn_3O_4@N-doped C in KOH, which further confirms the good electrochemical behavior of other electrolyte solutions. The Mn_3O_4@N-doped C exhibited higher cycling stability in KOH at a rate capability of 97.77%

https://doi.org/10.1021/acsomega.4c00676
ACS Omega 2024, 9, 17563−17576

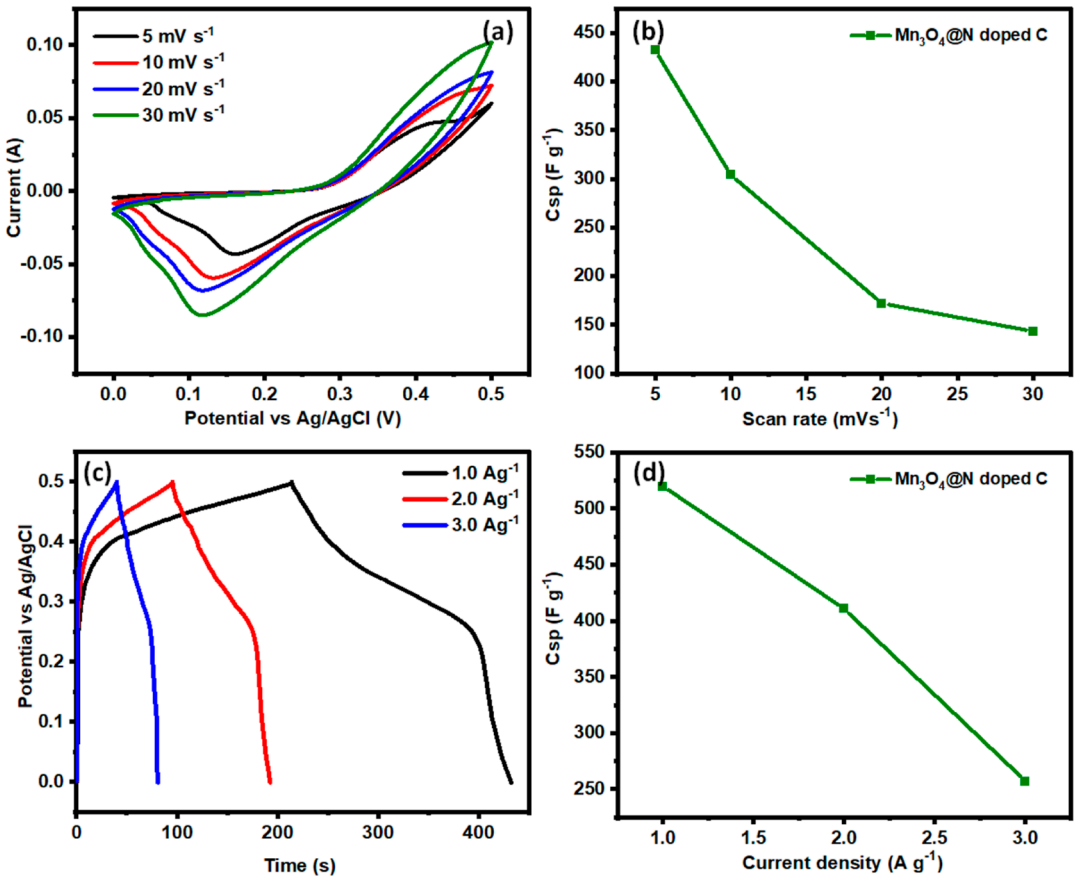

Figure 11. (a) CV profile, (b) C_s profile, (c) GCD plot, and (d) C_s from GCD of carbonized manganese oxide.

compared to other electrolyte solutions. To determine the real potential capability of the carbonized doped manganese oxide, an electrode system was conducted in KOH. The Mn_3O_4@ N-doped C displays a high C_s of 519 F g^{-1}, smaller than the three-electrode system. In light of the above found results, carbonized doped manganese oxide exhibited a higher electrochemical efficiency in KOH than another basic electrolytes. It was attributed to the higher ionic mobility, reduced hydration sphere of K^+, and low charge density. Our work shows that Mn_3O_4@ N-doped C is a suitable pseudocapacitive material for high-performance supercapacitors, in addition to verifying the practicality of rational design of enhanced integrated electrode materials.

■ ASSOCIATED CONTENT

Data Availability Statement

Data will be made available on reasonable request.

Supporting Information

The Supporting Information is available free of charge at https://pubs.acs.org/doi/10.1021/acsomega.4c00676.

Material analysis and electrochemical study (PDF)

■ AUTHOR INFORMATION

Corresponding Author

Salma Aman − *Institute of Physics, Khwaja Fareed University of Engineering and Information Technology, Rahim Yar Khan 64200, Pakistan;* orcid.org/0000-0001-5970-8036; Email: salma.physics.kfu@gmail.com

Authors

Amal F. Seliem − *Department of Chemistry, Faculty of Science and Arts, Najran University, Najran 61441, Saudi Arabia*

Ayeda Y. A. Mohammed − *Department of Chemistry, Faculty of Science and Arts, Najran University, Najran 61441, Saudi Arabia*

A. Attia − *Department of Chemistry, Faculty of Science and Arts, Najran University, Najran 61441, Saudi Arabia*

Naseeb Ahmad − *Institute of Physics, Khwaja Fareed University of Engineering and Information Technology, Rahim Yar Khan 64200, Pakistan*

Mohamed M. Ibrahim − *Department of Chemistry, College of Science, Taif University, Taif 21944, Saudi Arabia*

Complete contact information is available at: https://pubs.acs.org/10.1021/acsomega.4c00676

Author Contributions

All the authors have contributed to the work and they are known with the submission.

Notes

The authors declare no competing financial interest.

■ ACKNOWLEDGMENTS

The authors are thankful to the Deanship of Scientific Research at Najran University for funding this work under the Research Priorities and Najran Research funding program. grant code (NU/NRP/SERC/12/12).

REFERENCES

(1) Mishra, D.; Kim, S.; Kumar, N.; Krishnaiah, M.; Jin, S. H. Self-Discharge Mitigated Supercapacitors via Hybrid CuO-Nickel Sulfide Heterostructure for Energy Efficient, Wireless Data Storage Application. *J. Mater. Sci. Technol.* **2023**, *147*, 77−90.

(2) Javed, M. S.; Asim, S.; Najam, T.; Khalid, M.; Hussain, I.; Ahmad, A.; Assiri, M. A.; Han, W. Recent Progress in Flexible Zn-Ion Hybrid Supercapacitors: Fundamentals, Fabrication Designs, and Applications. *Carbon Energy* **2023**, *5* (1), No. e271.

(3) Deka, S. Nanostructured Mixed Transition Metal Oxide Spinels for Supercapacitor Applications. *Dalton Trans.* **2023**, *52*, 839−856.

(4) Mulik, S. V.; Dhas, S. D.; Moholkar, A. V.; Parale, V. G.; Park, H.-H.; Koyale, P. A.; Ghodake, V. S.; Panda, D. K.; Delekar, S. D. Square-Facet Nanobar MOF-Derived Co3O4@Co/N-Doped CNT Core−Shell-Based Nanocomposites as Cathode Materials for High-Performance Supercapacitor Studies. *ACS Omega* **2023**, *8*, 2183−2196.

(5) R, C.; Yadav, A. A. Spray-Deposited Cobalt-Doped RuO2 Electrodes for High-Performance Supercapacitors. *Electrochim. Acta* **2023**, *437*, 141521.

(6) Sun, W.; Chen, L.; Meng, S.; Wang, Y.; Li, H.; Han, Y.; Wei, N. Synthesis of NiO Nanospheres with Ultrasonic Method for Supercapacitors. *Mater. Sci. Semicond. Process.* **2014**, *17*, 129−133.

(7) Bhujun, B.; Tan, M. T. T.; Shanmugam, A. S. Evaluation of Aluminium Doped Spinel Ferrite Electrodes for Supercapacitors. *Ceram. Int.* **2016**, *42* (5), 6457−6466.

(8) Li, W.; Shao, J.; Liu, Q.; Liu, X.; Zhou, X.; Hu, J. Facile Synthesis of Porous Mn2O3 Nanocubics for High-Rate Supercapacitors. *Electrochim. Acta* **2015**, *157*, 108−114.

(9) Ma, Z.; Huang, X.; Dou, S.; Wu, J.; Wang, S. One-Pot Synthesis of Fe2O3 Nanoparticles on Nitrogen-Doped Graphene as Advanced Supercapacitor Electrode Materials. *J. Phys. Chem. C* **2014**, *118* (31), 17231−17239.

(10) Zhang, W.; Yin, Z.; Chun, A.; Yoo, J.; Diao, G.; Kim, Y. S.; Piao, Y. Rose Rock-Shaped Nano Cu2O Anchored Graphene for High-Performance Supercapacitors via Solvothermal Route. *J. Power Sources* **2016**, *318*, 66−75.

(11) Yu, L.; Shao, L.; Pan, R.; Guan, J.; Lin, J.; Shi, X.; Cai, J.; Sun, J.; Chen, C.; Wu, Y.; Sun, Z. Facile Development of Disused Nickel Foams into Low-Cost and High-Performance Electrode Materials for Sodium-Ion Batteries. *ACS Sustain. Chem. Eng.* **2023**, *11*, 10324−10332.

(12) Luo, J.; Shao, L.; Yu, L.; Shi, X.; Xu, J.; Sun, J.; Hang, L.; Wu, Y.; Sun, Z. Self-Intercalated Quasi-2D Structured V5Se8 Wrapped with Multi-Walled Carbon Nanotubes toward Advanced Sodium Ion Batteries. *Mater. Today Phys.* **2023**, *35*, 101099.

(13) Yu, L.; Shao, L.; Wang, S.; Guan, J.; Shi, X.; Cai, J.; Tarasenko, N.; Sun, Z. A Low-Cost NiSe2 Derived from Waste Nickel Foam as a High-Performance Anode for Sodium Ion Batteries. *Mater. Today Phys.* **2022**, *22*, 100593.

(14) Shi, X.; Liang, W.; Liu, G.; Chen, B.; Shao, L.; Wu, Y.; Sun, Z.; García, F. Electrode Materials for Li/Na Storage from Mechanochemically Synthesised MOFs/MXene Composites: A Solvent-Free Approach. *Chem. Eng. J.* **2023**, *462*, 142271.

(15) Liu, C.; Song, H.; Zhang, C.; Liu, Y.; Zhang, C.; Nan, X.; Cao, G. Coherent Mn3O4-Carbon Nanocomposites with Enhanced Energy-Storage Capacitance. *Nano Res.* **2015**, *8* (10), 3372−3383.

(16) Radhakanth, S.; Singhal, R. In−Situ Synthesis of MnO Dispersed Carbon Nanofibers as Binder-Free Electrodes for High-Performance Supercapacitors. *Chem. Eng. Sci.* **2023**, *265*, 118224.

(17) Yang, W.; Ni, M.; Ren, X.; Tian, Y.; Li, N.; Su, Y.; Zhang, X. Graphene in Supercapacitor Applications. *Curr. Opin. Colloid Interface Sci.* **2015**, *20* (5−6), 416−428.

(18) Querne, C.; Vignal, T.; Pinault, M.; Banet, P.; Mayne-L'Hermite, M.; Aubert, P. H. A Comparative Study of High Density Vertically Aligned Carbon Nanotubes Grown onto Different Grades of Aluminum − Application to Supercapacitors. *J. Power Sources* **2023**, *553*, 232258.

(19) Al Kiey, S. A.; Abdelhamid, H. N. Metal-Organic Frameworks (MOFs)-Derived Co3O4@N-Doped Carbon as an Electrode Materials for Supercapacitor. *J. Energy Storage* **2022**, *55*, 105449.

(20) Tholkappiyan, R.; Naveen, A. N.; Vishista, K.; Hamed, F. Investigation on the Electrochemical Performance of Hausmannite Mn3O4 Nanoparticles by Ultrasonic Irradiation Assisted Co-Precipitation Method for Supercapacitor Electrodes. *J Taibah Univ. Sci.* **2018**, *12* (5), 669−677.

(21) Wang, S.; Xiang, C.; Xiao, Z.; Xu, F.; Sun, L.; Zou, Y. Nickel-Molybdenum Metal Hydroxide Wrapped ZIF-67 for Supercapacitor Applications. *J. Energy Storage* **2023**, *59*, 106555.

(22) Liu, S.; Kang, L.; Jun, S. C. Challenges and Strategies toward Cathode Materials for Rechargeable Potassium-Ion Batteries. *Adv. Mater.* **2021**, *33*, 2004689.

(23) Kang, L.; Liu, S.; Zhang, Q.; Zou, J.; Ai, J.; Qiao, D.; Zhong, W.; Liu, Y.; Jun, S. C.; Yamauchi, Y.; Zhang, J. Hierarchical Spatial Confinement Unlocking the Storage Limit of MoS2 for Flexible High-Energy Supercapacitors. *ACS Nano* **2024**, *18*, 2149−2161.

(24) Qi, Z.; Younis, A.; Chu, D.; Li, S. A Facile and Template-Free One-Pot Synthesis of Mn3O4 Nanostructures as Electrochemical Supercapacitors. *Nano-Micro Lett.* **2016**, *8* (2), 165−173.

(25) Zhang, S.; Han, F.; Pan, Q.; Lin, D.; Zhu, X.; Shao, C.; Zhang, G.; Wang, Z.; Sun, S.; Meng, G.; Zhang, S.; Han, F.; Pan, Q.; Lin, D.; Meng, G.; Zhu, X.; Shao, C.; Wang, Z.; Zhang, G.; Sun, S. 3D Grid of Carbon Tubes with Mn₃O₄-NPs/CNTs Filled in their Inner Cavity as Ultrahigh-Rate and Stable Lithium Anode. *Energy Environ. Mater.* **2023**, *6*, No. e12586.

(26) Abdelhamid, H. N.; Al Kiey, S. A.; Sharmoukh, W. A High-Performance Hybrid Supercapacitor Electrode Based on ZnO/Nitrogen-Doped Carbon Nanohybrid. *Appl. Organomet. Chem.* **2022**, *36* (1), No. e6486.

(27) Sharmoukh, W.; Abdelhamid, H. N. Fenton-like Cerium Metal−Organic Frameworks (Ce-MOFs) for Catalytic Oxidation of Olefins, Alcohol, and Dyes Degradation. *J. Cluster Sci.* **2023**, *34* (5), 2509−2519.

(28) Horike, S.; Ma, N.; Fan, Z.; Kosasang, S.; Smedskjaer, M.; Mechanics, M. Mechanics, Ionics, and Optics of Metal−Organic Framework and Coordination Polymer Glasses. *Nano Lett.* **2021**, *21* (15), 6382−6390.

(29) Majidi, R.; Keramatinia, M.; Ramezanzadeh, B.; Ramezanzadeh, M. Weathering Resistance (UV-Shielding) Improvement of a Polyurethane Automotive Clear-Coating Applying Metal-Organic Framework (MOF) Modified GO Nano-Flakes (GO-ZIF-7). *Polym. Degrad. Stab.* **2023**, *207*, 110211.

(30) Sun, W.; Zhao, X.; Webb, E.; Xu, G.; Zhang, W.; Wang, Y. Advances in Metal−Organic Framework-Based Hydrogel Materials: Preparation, Properties and Applications. *J. Mater. Chem. A* **2023**, *11*, 2092−2127.

(31) Gu, J. F.; Chen, C.; Zheng, Z. H.; Hang, J.; Sang, W.; Wang, J. C.; Yuan, Y.; Chaemchuen, S.; Verpoort, F. Zeolitic Imidazolate Framework-8 as an Efficient and Facile Heterogeneous Catalyst for the Acceptorless Alcohol Dehydrogenation to Carboxylates. *J. Catal.* **2023**, *417*, 202−212.

(32) Gu, A.-L.; Zhang, Y.-X.; Wu, Z.-L.; Cui, H.-Y.; Hu, T.-D.; Zhao, B. Highly Efficient Conversion of Propargylic Alcohols and Propargylic Amines with CO2 Activated by Noble-Metal-Free Catalyst Cu2O@ZIF-8. *Angew. Chem.* **2022**, *134* (19), No. e202114817.

(33) Karimi, A.; Vatanpour, V.; Khataee, A.; Safarpour, M. Contra-Diffusion Synthesis of ZIF-8 Layer on Polyvinylidene Fluoride Ultrafiltration Membranes for Improved Water Purification. *J. Ind. Eng. Chem.* **2019**, *73*, 95−105.

(34) Wang, X.; Liu, J.; Leong, S.; Lin, X.; Wei, J.; Kong, B.; Xu, Y.; Low, Z. X.; Yao, J.; Wang, H. Rapid Construction of ZnO@ZIF-8 Heterostructures with Size-Selective Photocatalysis Properties. *ACS Appl. Mater. Interfaces* **2016**, *8* (14), 9080−9087.

(35) Aboraia, A. M.; Darwish, A. A. A.; Polyakov, V.; Erofeeva, E.; Butova, V.; Zahran, H. Y.; El-Rehim, A. A.; Algarni, H.; Yahia, I. S.; Soldatov, A. V. Structural Characterization and Optical Properties of

https://doi.org/10.1021/acsomega.4c00676
ACS Omega 2024, 9, 17563−17576

Zeolitic Imidazolate Frameworks (ZIF-8) for Solid-State Electronics Applications. *Opt. Mater.* **2020**, *100*, 109648.
(36) Hou, C.; Zhao, D.; Wang, Y.; Zhang, S.; Li, S. Preparation of Magnetic Fe3O4/PPy@ZIF-8 Nanocomposite for Glucose Oxidase Immobilization and Used as Glucose Electrochemical Biosensor. *J. Electroanal. Chem.* **2018**, *822*, 50−56.
(37) Jia, D.; Yang, Z.; Gu, W.; Liu, X. Manganese-Based Metal-Organic-Framework Derived Hydrophilic Cathode with Carbon Nanotubes Introduced for Long-Life and High-Performance Aqueous Zinc-Ion Battery. *J. Alloys Compd.* **2022**, *910*, 164876.
(38) Hu, X.; Lou, X.; Li, C.; Yang, Q.; Chen, Q.; Hu, B. Green and Rational Design of 3D Layer-by-Layer MnO<*sub*>*x*</*sub*> Hierarchically Mesoporous Microcuboids from MOF Templates for High-Rate and Long-Life Li-Ion Batteries. *ACS Appl. Mater. Interfaces* **2018**, *10* (17), 14684−14697.
(39) Beknalkar, S. A.; Teli, A. M.; Bhat, T. S.; Pawar, K. K.; Patil, S. S.; Harale, N. S.; Shin, J. C.; Patil, P. S. Mn3O4 Based Materials for Electrochemical Supercapacitors: Basic Principles, Charge Storage Mechanism, Progress, and Perspectives. *J. Mater. Sci. Technol.* **2022**, *130*, 227−248.
(40) Shewale, P. S.; Yun, K. S. Surface Modified Ni Wire Supported Flexible Asymmetric Supercapacitor of Mn3O4// PEDOT-PSS-MWCNT and Its Solar Charging for Self-Powered Cu-Doped ZnO Nanorods-Based UV Photodetector. *J. Alloys Compd.* **2022**, *911*, 164939.
(41) Wang, B. R.; Hu, Y.; Pan, Z.; Wang, J. MOF-Derived Manganese Oxide/Carbon Nanocomposites with Raised Capacitance for Stable Asymmetric Supercapacitor. *RSC Adv.* **2020**, *10* (57), 34403−34412.
(42) Zhao, K.; Lyu, K.; Liu, S.; Gan, Q.; He, Z.; Zhou, Z. Ordered Porous Mn3O4@N-Doped Carbon/Graphene Hybrids Derived from Metal−Organic Frameworks for Supercapacitor Electrodes. *J. Mater. Sci.* **2017**, *52* (1), 446−457.
(43) Chen, J.; Liu, B.; Cai, H.; Liu, S.; Yamauchi, Y.; Jun, S. C. Covalently Interlayer-Confined Organic−Inorganic Heterostructures for Aqueous Potassium Ion Supercapacitors. *Small* **2023**, *19* (4), 2204275.
(44) Sun, X.; Keywanlu, M.; Tayebee, R. Experimental and Molecular Dynamics Simulation Study on the Delivery of Some Common Drugs by ZIF-67, ZIF-90, and ZIF-8 Zeolitic Imidazolate Frameworks. *Appl. Organomet. Chem.* **2021**, *35* (11), No. e6377.
(45) Tayebee, R.; Fattahi Abdizadeh, M.; Erfaninia, N.; Amiri, A.; Baghayeri, M.; Kakhki, R. M.; Maleki, B.; Esmaili, E. Phosphotungstic Acid Grafted Zeolite Imidazolate Framework as an Effective Heterogeneous Nanocatalyst for the One-Pot Solvent-Free Synthesis of 3,4-Dihydropyrimidinones. *Appl. Organomet. Chem.* **2019**, *33* (8), No. e4959.
(46) Dou, X.; Keywanlu, M.; Tayebee, R.; Mahdavi, B. Simulation of Adsorption and Release of Doxepin onto ZIF-8 Including in Vitro Cellular Toxicity and Viability. *J. Mol. Liq.* **2021**, *329*, 115557.
(47) Narenji-Sani, F.; Tayebee, R.; Chahkandi, M. New Task-Specific and Reusable ZIF-like Grafted H6P2W18O62 Catalyst for the Effective Esterification of Free Fatty Acids. *ACS Omega* **2020**, *5*, 9999−10010.
(48) Sun, G.; Xie, H.; Ran, J.; Ma, L.; Shen, X.; Hu, J.; Tong, H. Rational Design of Uniformly Embedded Metal Oxide Nanoparticles into Nitrogen-Doped Carbon Aerogel for High-Performance Asymmetric Supercapacitors with a High Operating Voltage Window. *J. Mater. Chem. A* **2016**, *4* (42), 16576−16587.
(49) Ma, L.; Sun, G.; Ran, J.; Lv, S.; Shen, X.; Tong, H. One-Pot Template-Free Strategy toward 3D Hierarchical Porous Nitrogen-Doped Carbon Framework in Situ Armored Homogeneous NiO Nanoparticles for High-Performance Asymmetric Supercapacitors. *ACS Appl. Mater. Interfaces* **2018**, *10* (26), 22278−22290.
(50) Li, Z.; Zhang, L. Y.; Zhang, L.; Huang, J.; Liu, H. ZIF-67-Derived CoSe/NC Composites as Anode Materials for Lithium-Ion Batteries. *Nanoscale Res. Lett.* **2019**, *14* (1), 358−411.
(51) Kümbetlioğlu, F.; Oskay, K. O.; Çıplak, Z.; Ateş, A. Preparation, Characterization, and Application of Metal Oxide-Doped Zeolitic Imidazolate Framework. *ACS Omega* **2023**, *8*, 27650−27662.
(52) Zheng, X.; Han, X.; Zhao, X.; Qi, J.; Ma, Q.; Tao, K.; Han, L. Construction of Ni-Co-Mn Layered Double Hydroxide Nanoflakes Assembled Hollow Nanocages from Bimetallic Imidazolate Frameworks for Supercapacitors. *Mater. Res. Bull.* **2018**, *106*, 243−249.
(53) Yao, J.; He, M.; Wang, K.; Chen, R.; Zhong, Z.; Wang, H. High-Yield Synthesis of Zeolitic Imidazolate Frameworks from Stoichiometric Metal and Ligand Precursor Aqueous Solutions at Room Temperature. *CrystEngComm* **2013**, *15* (18), 3601−3606.
(54) Zhang, Y.; Wu, M.; Kwok, Y. H.; Wang, Y.; Zhao, W.; Zhao, X.; Huang, H.; Leung, D. Y. C. In-Situ Synthesis of Heterojunction TiO2/MnO2 Nanostructure with Excellent Performance in Vacuum Ultraviolet Photocatalytic Oxidation of Toluene. *Appl. Catal., B* **2019**, *259*, 118034.
(55) Vadiyar, M. M.; Bhise, S. C.; Patil, S. K.; Kolekar, S. S.; Chang, J. Y.; Ghule, A. V. Comparative Study of Individual and Mixed Aqueous Electrolytes with ZnFe2O4 Nano−Flakes Thin Film as an Electrode for Supercapacitor Application. *ChemistrySelect* **2016**, *1* (5), 959−966.
(56) Zhong, S.; Zhan, C.; Cao, D. Zeolitic Imidazolate Framework-Derived Nitrogen-Doped Porous Carbons as High Performance Supercapacitor Electrode Materials. *Carbon* **2015**, *85*, 51−59.
(57) Gao, P.; Shen, B.; Zhao, P.; Shi, G.; Zhao, X. Tuning the Mn2+/Mn3+ Ratio of ZnMn2O4 from Spent Zinc-Carbon Battery Powder to Enhance the Electrochemical Performance. *J. Power Sources* **2023**, *577*, 233231.
(58) Chameh, B.; Moradi, M.; Kaveian, S. Synthesis of Hybrid ZIF-Derived Binary ZnS/CoS Composite as High Areal-Capacitance Supercapacitor. *Synth. Met.* **2020**, *260*, 116262.
(59) Otun, K. O.; Xaba, M. S.; Zong, S.; Liu, X.; Hildebrandt, D.; El-Bahy, S. M.; Alotaibi, M. T.; El-Bahy, Z. M. ZIF-8-Derived ZnO/C Decorated Hydroxyl-Functionalized Multi-Walled Carbon Nanotubes as a New Composite Electrode for Supercapacitor Application. *Colloid Interface Sci. Commun.* **2022**, *47*, 100589.
(60) Shrivastav, V.; Sundriyal, S.; Goel, P.; Saha, A.; Tiwari, U. K.; Deep, A. A Novel Zinc Sulfide Impregnated Carbon Composite Derived from Zeolitic Imidazolate Framework-8 for Sodium-Ion Hybrid Solid-State Flexible Capacitors. *Nanoscale Adv.* **2021**, *3* (21), 6164−6175.
(61) Wang, D.; Chen, Y.; Wang, H.; Zhao, P.; Liu, W.; Wang, Y.; Yang, J. N-Doped Porous Carbon Anchoring on Carbon Nanotubes Derived from ZIF-8/Polypyrrole Nanotubes for Superior Supercapacitor Electrodes. *Appl. Surf. Sci.* **2018**, *457*, 1018−1024.
(62) Zhu, Z.; Wang, Z.; Yan, Z.; Zhou, R.; Wang, Z.; Chen, C. Facile Synthesis of MOF-Derived Porous Spinel Zinc Manganese Oxide/Carbon Nanorods Hybrid Materials for Supercapacitor Application. *Ceram. Int.* **2018**, *44* (16), 20163−20169.
(63) Cai, W.; Kankala, R. K.; Xiao, M.; Zhang, N.; Zhang, X. Three-Dimensional Hollow N-Doped ZIF-8-Derived Carbon@MnO2 Composites for Supercapacitors. *Appl. Surf. Sci.* **2020**, *528*, 146921.
(64) Yan, Y.; Lin, J.; Xu, T.; Liu, B.; Huang, K.; Qiao, L.; Liu, S.; Cao, J.; Jun, S. C.; Yamauchi, Y.; Qi, J. Atomic-Level Platinum Filling into Ni-Vacancies of Dual-Deficient NiO for Boosting Electrocatalytic Hydrogen Evolution. *Adv. Energy Mater.* **2022**, *12* (24), 2200434.
(65) Malaie, K.; Ganjali, M. R.; Soavi, F. Toward Low-Cost and Sustainable Supercapacitor Electrode Processing: Simultaneous Carbon Grafting and Coating of Mixed-Valence Metal Oxides by Fast Annealing. *Front. Chem.* **2019**, *7*, 430211.
(66) Yan, Y.; Lin, J.; Huang, K.; Zheng, X.; Qiao, L.; Liu, S.; Cao, J.; Jun, S. C.; Yamauchi, Y.; Qi, J. Tensile Strain-Mediated Spinel Ferrites Enable Superior Oxygen Evolution Activity. *J. Am. Chem. Soc.* **2023**, *145* (44), 24218−24229.
(67) Shao, Y.; Fu, J. H.; Cao, Z.; Song, K.; Sun, R.; Wan, Y.; Shamim, A.; Cavallo, L.; Han, Y.; Kaner, R. B.; Tung, V. C. 3D Crumpled Ultrathin 1T MoS2for Inkjet Printing of Mg-Ion Asymmetric Micro-Supercapacitors. *ACS Nano* **2020**, *14* (6), 7308−7318.

https://doi.org/10.1021/acsomega.4c00676
ACS Omega 2024, 9, 17563−17576

(68) Althubiti, N. A.; Hassan, M. M.; Waheed, M. S.; Aman, S.; Khosa, R. Y.; Farid, H. M. T.; Nazir, A.; Ansari, M. Z.; Abdulaziz, F.; Taha, T. A. M. Fabrication of Novel Zinc Selenide/Cadmium Oxide Nanohybrid Electrode via Hydrothermal Route for Energy Storage Application. *J. Energy Storage* **2023**, *70*, 108154.

https://doi.org/10.1021/acsomega.4c00676
ACS Omega 2024, 9, 17563−17576